

# Multi-wavelength investigations of co-evolution of bright cluster galaxies and their host clusters

Yasuhiro Hashimoto<sup>1\*</sup> J. Patrick Henry<sup>2,3</sup> and Hans Boehringer<sup>3</sup>

<sup>1</sup>*Department of Earth Sciences, National Taiwan Normal University No.88, Sec. 4, Tingzhou Rd., Wenshan District, Taipei 11677, Taiwan R.O.C*

<sup>2</sup>*Institute for Astronomy, University of Hawaii, 2680 Woodlawn Drive, Honolulu, Hawaii 96822, USA*

<sup>3</sup>*Max-Planck-Institut für extraterrestrische Physik, Giessenbachstrasse D-85748 Garching, Germany*

Accepted 2014 February 14

## ABSTRACT

We report a systematic multi-wavelength investigation of environments of the brightest cluster galaxies (BCGs), using the X-ray data from the Chandra archive, and optical images taken with  $34' \times 27'$  field-of-view Subaru Suprime-Cam. Our goal is to help understand the relationship between the BCGs and their host clusters, and between the BCGs and other galaxies, to eventually address a question of the formation and co-evolution of BCGs and the clusters.

Our results include: 1) Morphological variety of BCGs, or the second or the third brightest galaxy (BCG2, BCG3), is comparable to that of other bright red sequence galaxies, suggesting that we have a continuous variation of morphology between BCGs, BCG2, and BCG3, rather than a sharp separation between the BCG and the rest of the bright galaxies. 2) The offset of the BCG position relative to the cluster centre is correlated to the degree of concentration of cluster X-ray morphology (Spearman  $\rho = -0.79$ ), consistent with an interpretation that BCGs tend to be off-centered inside dynamically unsettled clusters. 3) Morphologically disturbed clusters tend to harbour the brighter BCGs, implying that the “early collapse” may not be the only major mechanism to control the BCG formation and evolution.

**Key words:** Galaxies: clusters: general – X-rays: galaxies: clusters – Galaxies: evolution

## 1 INTRODUCTION

It has been known for several decades that a significant fraction of galaxy clusters show disturbed cluster morphologies, indicative of possible recent mergers (e.g. Geller & Beers 1982; Dressler & Shectman 1988). In addition to the obvious interest in the merger phenomena themselves, the important connection between the morphologies of galaxy clusters and the properties of member galaxies has also received much attention (e.g. Butcher & Oemler 1978; Caldwell et al. 1993; Metevier et al. 2000; Gerke et al. 2007). This connection has generally been formulated in terms of the frequency of ‘structure’ in clusters and from qualitative measures of the properties of the member galaxies.

Methods to quantify cluster structures at optical wavelengths have mostly used both the distribution of cluster galaxies, and lensing. The distribution studies analyze, either visually or objectively, the substructure in 1D, 2D

or sometimes 3D, depending on the level of information available (e.g. Geller & Beers 1982; Dressler & Shectman 1988; Rhee et al. 1992; Bird 1994; Kriessler & Beers 1997). Bautz & Morgan (1970) classified cluster morphology based on visual inspection of optical images, by the degree to which the brightest cluster member stands out against the cluster background. The RS system (Rood & Sastry 1971; Struble & Rood 1984, 1987) is based on the projected distribution of the brightest galaxies in the cluster. The RS system is composed of six major classes: cD, B, C, L, F, and I-type clusters. These six classes have been interpreted as corresponding to a sequence of cluster evolution (Forman & Jones 1982; Struble & Rood 1984). Butcher & Oemler (1984) characterized the optical morphology of cluster by the degree of central concentration of galaxy distribution. Their concentration is defined by  $\log(R_{60}/R_{20})$  where  $R_{60}$  or  $R_{20}$  is the radius of the circle containing 60% or 20% of the cluster projected galaxy distribution, respectively.

\* Email: hashimot@ntnu.edu.tw

An alternative method comes from X-ray wavelengths,

because cluster mergers compress and heat the intracluster gas, and this can be measured as distortions of the spatial distribution of X-ray surface brightness and temperature. Jones & Forman (1999) visually examined 208 clusters observed with *Einstein* X-ray satellite and separated these clusters into six morphological classes. Meanwhile, using the *Einstein* images, Mohr et al. (1995) measured emission-weighted centroid variation, axial ratio, orientation, and radial falloff for a sample of 65 clusters, while several other studies used ellipticity (e.g. Kolokotronis et al. 2001; Melott et al. 2001; Plionis 2002). Buote & Tsai (1995, 1996) used a power ratio method for 59 low redshift clusters observed with *ROSAT*, and Jeltema et al. (2005) have extended the method to 40 clusters at  $z=0.15-0.9$  using *Chandra* data. Schuecker et al. (2001) conducted a study of 470 clusters from the *ROSAT*-ESO Flux-Limited X-ray (REFLEX) cluster survey (Böhringer et al. 2001) using sophisticated statistics, such as Fourier elongation test, Lee test, and  $\beta$  test. Hashimoto et al. (2007) studied X-ray cluster morphology using a sample of 101 clusters of galaxies at redshift  $z\sim 0.05-1$  taken from the Chandra archive. There, X-ray morphology is quantitatively characterized by a series of objectively measured simple statistics, such as concentration, asymmetry, elongation, and off-centerness of the X-ray surface brightness distribution. These measures are designed to be robust against variations of image quality caused by various exposure times and various cluster redshifts.

Quantifying cluster structures by investigating the distribution of cluster galaxies in optical wavelengths requires a large number of galaxies, and is more susceptible to contamination from foreground and background objects. Lensing study in optical wavelengths is also sensitive to this contamination, and does not have good spatial resolution except for the central region of a cluster. The X-ray method is superior against fore/background because X-ray emissivity is proportional to the square of the electron density, and therefore less affected by the superposed structures than optical data. Meanwhile, the advantage of using optical data is the size of the available cluster catalogs, which can be much larger than those originating from X-ray data. Optical and X-ray characteristics of cluster structures are complementary, and by the systematic comparison between X-ray and optical methods, one may calibrate and evaluate different sensitivity and bias between the optical and X-ray characteristics of clusters (e.g. Hashimoto et al. 2007b).

There are numerous studies investigating the relationship between the galaxy properties and their host clusters (as well as smaller scale environments, such as the local density). The galaxy properties investigated range from the colour and morphology to the star formation properties of galaxies (e.g. Butcher & Oemler 1978; Dressler 1980; Hashimoto et al. 1998; Hashimoto & Oemler Jr 1999; Goto et al. 2003). Unfortunately, most of these studies only uses the optical band to characterize the clusters. Only a handful of studies uses multi-band information from both optical and X-ray data (e.g. Edge & Stewart 1991; Metevier et al. 2000; Hashimoto et al. 2008). These studies are important, however, a more systematic investigation of cluster galaxies using multi-wavelength data in a coherent manner is much needed.

Among all cluster galaxies, the brightest cluster galaxies (BCGs) are a unique class of objects. Despite their apparent

morphological resemblance to elliptical galaxies, BCGs tend to have lower surface brightness (e.g. von der Linden et al. 2007), while their spatial extent is much larger (effective radius  $\sim 30$  kpc) than ordinary elliptical galaxies (e.g. Schneider et al. 1983; Schombert 1986; Gonzalez et al. 2005). Meanwhile, BCGs tend to have smaller velocity dispersions and smaller colour gradients in their radial profiles (Bernardi et al. 2011). BCGs also tend to lie close to the center of cluster in both 2-d and velocity space (e.g. Quintana & Lawrie 1982; Oegerle & Hill 2001), implying that they are often located at the minimum in the cluster potential well, thus their formation history may have been dominated by different physical processes compared to the other galaxies in the clusters.

According to the cold dark matter model, BCGs form hierarchically by the merging of smaller galaxies, and the formation history of the BCG is closely linked to that of the host cluster (e.g. De Lucia & Blaizot 2007). Indeed, observationally, it has been found that BCGs' properties are closely related to those of host clusters: a significant alignment between the elongations of BCGs and their host clusters is observed in both the optical (Carter & Metcalfe 1980; Struble 1990; Plionis et al. 2003) and X-ray bands (Hashimoto et al. 2008). The correlation between the BCG luminosity and various optical cluster properties are also found (e.g. Oemler Jr 1976; Schombert 1987; Lin & Mohr 2004). The BCG luminosity is also found to be weakly correlated to cluster X-ray temperature or luminosity (e.g. Schombert 1987; Edge & Stewart 1991; Brough et al. 2002; Katayama et al. 2003).

The unique characters of BCGs allows us to use them as important diagnostics of the dynamical status of the host clusters. One of the most important example is that the offset between the BCG and the center of global cluster potential well is expected to be sensitive to the cluster dynamical state (e.g. Ostriker & Tremaine 1975; Merritt 1985; Katayama et al. 2003). Beers & Geller (1983) investigated the offset of cD galaxy from the peak of the galaxy surface density, using a sample of 55 nearby rich clusters of galaxies. They found that cD galaxies often do not lie at the global center of the galaxy surface distribution. They suggested that these galaxies tend to lie at the bottom of *local* potential wells, rather than global potential wells. The offset of cD (and D) galaxies with respect to the host clusters in velocity space is also reported (Malumuth et al. 1992; Zabludoff et al. 1993; Bird 1994; Oegerle & Hill 2001).

These results suggest that BCGs may not always be at the bottom of the global potential well of their host clusters. However, these previous studies quantifying cluster structures by the galaxy surface density were unfortunately sensitive to fore/background contamination. Even if one uses spectroscopic/photometric redshifts to help identify cluster members, determining the center from the galaxy surface density often lacks the spatial resolution, because the redshift information (particularly, those of spectroscopic redshifts) are not provided for all cluster galaxies. Even if we could have complete cluster membership information for all galaxies, we still have an intrinsically limited spatial resolution because each galaxy itself can act as a discrete noise, particularly after discarding the BCG from the galaxy distribution.

X-ray is superior for determining cluster structure, such

as the center of the cluster, because it is less affected by the superposed structure than optical bands. Several researchers (e.g. Katayama et al. 2003; Sanderson et al. 2009) investigated the offset between BCG and X-ray centroid for nearby clusters, and confirmed a correlation between the BCG offset and presence of cool core, or radio emission. Unfortunately, most previous studies are predominantly using the cluster sample that consists of low redshift bright clusters, that preferentially contains dynamically settled clusters. Therefore, the effect of cluster dynamical status on the luminosity (or other properties) of BCGs were hardly addressed. Furthermore, despite the large number of previous work, the nature of formation of the BCGs, in particular, whether or not the BCGs are special, rather than representing the extreme bright end of the normal galaxy populations, is an open question. It is unclear whether or not various ‘features’ discovered among BCGs can be explained as ‘continuous’ extension of normal galaxies, or represent discrete signature to separate BCGs from other galaxies.

Unfortunately, in the large majority of previous studies comparing the properties of clusters and BCGs or generic cluster member galaxies, the cluster properties were characterized predominantly in optical/NIR bands based on the galaxy surface density. Even if the X-ray was additionally used to characterize cluster properties, they are typically just global X-ray luminosity or temperature, and no detailed X-ray analysis was conducted. Meanwhile, for a small number of studies where the X-ray was the ‘main’ waveband used to characterize the detailed *cluster* properties, complementary optical/NIR datasets, if any, for characterizing BCGs and other galaxies were often shallow, and assembled from observations with several telescopes. Finally, in these ‘X-ray main’ studies, clusters are typically selected from the nearby X-ray bright cluster sample and/or dynamically settled clusters. Therefore, the effect of cluster dynamical status on the luminosity (or other properties) of BCGs could not be well addressed.

What is needed is to investigate cluster properties and member galaxies in a coherent manner across the wavebands, using homogeneous datasets covering a wide range of cluster properties. The optical datasets should ideally be simultaneously wide and deep, while the X-ray data should be both sensitive and with good spatial resolution so that one can perform detailed dynamical analysis of distant clusters, based on the X-ray cluster morphologies, free from the effect of contaminating point sources.

We are conducting a new investigation of the relationship between the cluster properties and the member galaxy properties, where the properties of galaxies are characterized based on optical images taken with the large field of view Suprime-Cam (Miyazaki et al. 1998) on the Subaru 8m telescope, while cluster properties are determined by the high spatial resolution X-ray data taken from the Chandra ACIS archive. We will conduct a systematic multi-band investigation to study the relationship between the clusters and their member galaxies in a wide range of cluster properties, such as dynamical status, cluster redshifts, and in a wide range of galaxies properties, from core to outskirts, and from bright to faint galaxies.

In this paper, we report the investigation of relationship between cluster properties and the brightest cluster galaxies (BCGs). Our goal is to help understand the formation and

evolution of BCGs, including the relationship between the BCGs and their host clusters, and between the BCGs and other galaxies, to eventually address a question of whether or not the BCGs are special, rather than representing the extreme bright end of the normal galaxy populations.

This paper is organized as follows. In Sec. 2 & 3, we describe our sample and our measures, and in Sec. 4, systematics and deblending are described, and Sec. 5 summarizes our results. Throughout the paper, we use  $H_0 = 70 \text{ km s}^{-1} \text{ Mpc}^{-1}$ ,  $\Omega_m = 0.3$ , and  $\Omega_\Lambda = 0.7$ , unless otherwise stated.

## 2 X-RAY DATA AND MEASURES

Here we briefly summarize our sample, X-ray data preparation, and X-ray measures. We have used a sample defined in Hashimoto et al. (2007) where almost all clusters are selected from flux-limited X-ray surveys, and X-ray data are taken from the Chandra ACIS archive. A lower limit of  $z = 0.05$  or  $0.1$  is placed on the redshift to ensure that a cluster is observed with sufficient field-of-view with ACIS-I or ACIS-S, respectively. The majority of our sample comes from the *ROSAT* Brightest Cluster Sample (BCS; Ebeling et al. 1998) and the Extended *ROSAT* Brightest Cluster Sample (EBCS; Ebeling et al. 2000). To extend our sample to higher redshifts, additional high- $z$  clusters are selected from various deep surveys including: *ROSAT* Deep Cluster Survey (RDCS; Rosati et al. 1998), *Einstein* Extended Medium Sensitivity Survey (EMSS; Gioia et al. 1990; Henry et al. 1992), and 160 Square Degrees *ROSAT* Survey (Vikhlinin et al. 1998).

The resulting sample contains 120 clusters. At the final stage of our data processing, to employ our full analysis, we further applied a selection based on the total counts of cluster emission, eliminating clusters with very low signal-to-noise ratio. Clusters whose center is too close to the edge of the ACIS CCD are also removed. The resulting final sample contains 101 clusters with redshifts between 0.05 - 1.26 (median  $z = 0.226$ ). We reprocessed the level=1 event file retrieved from the archive. The data were filtered to include only the standard event grades 0,2,3,4,6 and status 0, then multiple pointings were merged, if any. We eliminated time intervals of high background count rate by performing a  $3\sigma$  clipping of the background level. We corrected the images for exposure variations across the field of view, detector response and telescope vignetting.

We detected point sources using the CIAO routine `celldetect` with a signal-to-noise threshold for source detection of three. An elliptical background annulus region was defined around each source such that its outer major and minor axes were three times the size of the source region. We removed point sources, except for those at the center of the cluster which was mostly the peak of the surface brightness distribution rather than a real point source. The images were then smoothed with Gaussian  $\sigma=5''$ . We decided to use isophotal contours to characterize an object region, instead of a conventional circular aperture, because we did not want to introduce any bias in the shape of an object. To define constant metric scale to all clusters, we adjusted an extracting threshold in such a way that the square root of the detected object area times a constant was 0.5 Mpc, i.e.  $\text{const}\sqrt{\text{area}} = 0.5 \text{ Mpc}$ . We chose  $\text{const} = 1.5$ , because the

isophotal limit of a detected object was best represented by this value.

Morphology of individual cluster is objectively characterized by measures, such as, ellipticity, asymmetry, and concentration. The ellipticity is defined by the ratio of semi-major and semi-minor axis. The asymmetry is measured by first rotating an image by 180 degrees around the object center, then subtracting the rotated image from the original unrotated one. The residual signals above zero are summed and then normalized. The degree of concentration of the surface brightness profile is defined by the ratio between central 30% and whole 100% elliptical apertures. (For further detail of the sample and measures, please see Hashimoto et al. 2007).

### 3 OPTICAL DATA AND MEASURES

The optical broad band images taken with Suprime-Cam on the Subaru telescope, were retrieved from Subaru-Mitaka-Okayama-Kiso Archive (SMOKA). Reduction software developed by Yagi et al. (2002) was used for flat-fielding, instrumental distortion correction, differential refraction, sky subtraction, and stacking. The camera covers a  $34' \times 27'$  field of view with a pixel scale of  $0''.202$ . The photometry is calibrated to Vega system using SDSS dr8, and transformation from Jordi & Ammon (2006) were used to obtain the zero points. For observations without corresponding SDSS data, Landolt standards (Landolt 1992), if any, were used. Data taken under possible non-photometric conditions (estimated by the derived magnitude zero-point versus exposure time plane) are discarded unless we can perform direct calibration using standard stars in and all over the same field of view. Accuracy of photometry is approximately 0.1 mag. The Galactic extinction is corrected using the extinction map of Schlegel et al. (1998). K-correction is calculated based on the polynomial approximation of Chilingarian et al. (2010), where they compare their approximation to spectral based k-correction by Roche et al. (2009) and SED based k-correction by KCORRECT (Blanton & Roweis 2007) for a consistency check. The k-correction for the bulk of our BCG is less than 0.5, 0.4, and 0.25, respectively for R, I+, and Z band. Extrapolating the polynomial to  $z \sim 1.0$  may require a bit of care, although in 'redder' bands, such as R, I, and Z, k-correction behaves relatively well even at these redshifts. As a precaution, however, we compare the polynomial to another analytical approximation for E/SO galaxies in R band by Jorgensen et al. (1992) in a form of  $k \sim 2.5(1+z)$  for consistency. K-correction for  $z \sim 1$  is about  $\sim 0.7$ . Based on the residuals Chilingarian et al. (2010), we roughly estimate our k-correction uncertainty to be about 0.1, 0.05, and 0.05, respectively in R, I+, and Z band for our early type galaxies at  $z < 0.5$ , and about 0.2, 0.1, and 0.1 for the galaxies at  $z \sim 1$ .

We refine the original astrometry written as WCS keyword in the distributed archival data using the USNO-A2 catalog with positional uncertainties less than  $\sim 0.2''$ . The data were taken under various seeing conditions, and we used only images with less than  $\sim 1''.2$  seeing. The optical data retrieved from SMOKA contains 66 clusters with redshifts between 0.08 - 1.13.

Objects are detected in the 'detection' band for each cluster, which is determined by the cluster redshift and data availability. Total global effective exposure time after the filtering, the detection wavebands, and other information are summarized in Table 1. Object detection is performed using SExtractor (Bertin & Arnouts 1996). We used MAG\_AUTO for total magnitudes, and 2" aperture magnitudes for colours, if applicable. Star-galaxy separation is performed on the basis of CLASS\_STAR versus total magnitude diagram.

We selected BCG as the brightest in the detection band inside a projected radius of 0.5 Mpc from the X-ray center. BCG is then visually inspected and the assignment is, if it is necessary, adjusted, in light of the BCG morphology and distance to the X-ray center. The morphology of BCGs and other generic galaxies are objectively characterized in a homogeneous fashion using similar measures as the X-ray analysis, including ellipticity, asymmetry, and concentration. Note that the concentration used in the X-ray analysis is optimized to cluster X-ray profile, therefore, if it is applied to the galaxy profile, it is too sensitive to the outer faint structure, and thus to the variation of detection/analysis threshold. There are many variants of concentration measures characterizing the galaxy profile (e.g. Okamura et al. 1984; Doi et al. 1993; Abraham et al. 1994; Hashimoto et al. 1998; Hashimoto & Oemler Jr 1999; Conselice 2003; Goto et al. 2003), where the concentration (or 'inverse' concentration) is defined as the ratio of the light inside a certain inner radius to the light inside a certain outer radius, or the ratio between the inner and the outer radii. We have tested several concentration measures, and have decided to use the radius ratio, rather than the flux ratio, taking Petrosian 50 percent radius as the inner radius, and Petrosian 90 percent as the outer radius, which are relatively robust against various analysis thresholds for the typical galaxy light profile. Petrosian 50 percent or 90 percent radius is the radius at which the ratio of the local surface brightness in an annulus at  $r$  to the mean surface brightness within  $r$  is 0.5 or 0.9, respectively (c.f. Yasuda et al. 2001). The concentration is then defined by the outer radius divided by the inner radius, which is somewhat similar to the *inverse* of the 'SDSS inverse concentration' (e.g. Goto et al. 2003). Apart from the concentration index, there are several parameters that are measured only for characterizing the galaxy structures: a 'contrast' parameter is measured by taking the ratio between the sum of light belonging to the top 30% brightest pixels and the total light belonging to an entire object. This contrast parameter, when normalized by the concentration, is designed to measure 'blubbiness' of the light distribution, similar to 'Clumpiness' (Conselice 2003). A series of the power ratios (e.g. Buote & Tsai 1996) that measure the square of the ratio of higher-order multipole moments of the two-dimensional potential to the monopole moment are also tested, although they, especially PW2 and PW3, are essentially similar to conventional measures such as the ellipticity and asymmetry.

**Table 1.** Summary of Subaru cluster data

Cluster	z (redshift)	filter <sup>a</sup>	exptime <sup>b</sup> (sec)	fov (arcmin)
3C295	0.46	R	960	26.3x33.2
A115	0.1971	I+	3600	35.1x27.7
A1201	0.1688	I+	2160	35.1x26.5
A1204	0.1904	I+	2160	35.3x28.4
A1413	0.1413	R	4800	35.1x28.1
A1423	0.213	I+	3840	35.1x28.7
A1682	0.226	I+	2160	34.8x29.2
A1689	0.184	I+	2160	35.9x28.5
A1758	0.28	R	2880	34.9x27.2
A1763	0.2279	I+	2160	35.4x29.0
A1835	0.258	I+	2400	34.7x25.8
A1914	0.1712	R	2880	33.5x27.6
A2034	0.11	R	2880	32.3x26.6
A2069	0.1145	R	900	26.4x28.7
A2111	0.211	I+	2880	34.8x29.2
A2204	0.152	R	540	28.0x28.1
A2218	0.171	I+	1500	36.0x28.6
A2219	0.2281	R	1440	31.9x28.0
A2255	0.0798	R	2520	34.5x28.8
A2259	0.164	I+	2160	35.3x26.9
A2261	0.224	R	1620	26.2x31.6
A2319	0.0564	R	2835	34.2x26.8
A2390	0.233	R	1620	26.8x35.5
A2409	0.1470	I+	2160	35.3x29.3
A2552	0.299	R	1680	26.2x34.2
A267	0.23	I+	2640	32.6x25.6
A370	0.357	I+	1800	35.0x28.9
A520	0.203	I+	1440	33.9x27.5
A586	0.171	I+	2100	35.1x26.4
A611	0.288	I+	2100	34.8x27.8
A68	0.2546	I+	2400	34.5x27.0
A697	0.282	I+	2400	34.0x27.3
A750	0.163	I+	1680	34.6x26.2
A754	0.0528	R	2880	33.5x26.0
A773	0.217	I+	4320	35.3x29.4
A781	0.2984	I+	2160	35.3x29.0
A963	0.206	R	3240	26.6x26.4
Hercules	0.154	I+	2160	35.3x28.5
CL0016	0.541	I+	3600	33.8x25.4
MS0451	0.54	I+	2280	28.6x35.1
MS1054	0.83	Z+	3600	34.5x27.9
MS1359	0.328	I+	1800	35.4x15.5
MS2053	0.583	I+	3600	35.4x26.1
RXJ0152	0.835	Z+	5220	35.3x27.4
RXJ0848B	0.57	I+	2160	35.0x26.6
RXJ0848†	1.27	Z+	4080	34.9x29.3
RXJ0849†	1.26	Z+	4080	34.9x29.3
RXJ0910†	1.106	Z+	1800	34.5x27.5
RXJ1054	1.134	Z+	3360	34.7x27.4
RXJ1252	1.235	Z+	3300	34.9x28.1
RXJ1347	0.451	I	1800	29.2x28.4
RXJ1532	0.3615	I	2160	28.4x32.4
RXJ1716	0.813	Z+	3040	34.8x27.9
RXJ1720	0.164	R	1440	26.8x32.9
RXJ2129	0.235	R	1620	28.6x27.0
RXJ2228	0.412	I	1620	32.3x27.9
WGA1226	0.89	Z+	1080	27.9x33.2
ZWCL0024	0.39	R	5280	35.9x26.2
ZWCL1883	0.194	I	2100	34.6x28.7
ZWCL1953	0.3737	I+	450	33.5x26.8
ZWCL2661	0.3825	R	2880	28.5x26.8
ZWCL2701	0.214	I+	2160	35.3x28.5
ZWCL3146	0.2906	I+	1440	34.8x17.7
ZWCL3959	0.3518	I	2160	34.2x29.0
ZWCL5247	0.229	I+	2160	35.3x29.2
ZWCL7160	0.2578	I+	3600	35.6x28.2

a: detection filter, filters marked with '+' are SDSS filters, without '+' are Johnson-Cousins filters; b: effective exposure time; †: clusters with no obvious BCGs (excluded from the analyses related to BCGs)

## 4 SYSTEMATICS AND DEBLENDING

### 4.1 Systematics

One of the important, yet unfortunately often lightly treated, problems associated with comparison of complex morphological characteristics of astronomical objects, galaxies or clusters, is the possible systematics introduced by various data quality, exposure times and object redshifts. Depending on the sensitivity of measures of characteristics, some susceptible measures may be seriously affected by these systematics, producing misleading results.

Unfortunately, investigating the systematics on the complex characteristics is not an easy task. To investigate the systematic effect of, for example, various exposure times, one of the standard approaches is to simulate an image with a given exposure time by using an exposure-time-scaled and noise-added model image. We need to approximate the various model characteristics to the complicated characteristics

of a real object. Unfortunately, those characteristics of the real objects are often what we want to investigate, and thus assuming what we want to measure is an almost impossible task.

Meanwhile, if we use real data, instead of a model, we will not have this problem. However, the standard simple ‘rescaling and adding-noise’ process to simulate a shorter exposure time will produce an image containing an excessive amount of Poisson noise for a given exposure time because of the intrinsic noise already presented in the original data, thus lead us to underestimate the data quality. This intrinsic noise is difficult to be removed even if we sacrifice the fine spatial details of an object by smoothing, because these smoothing will introduce yet another noise by correlating noises.

Similarly, to investigate the effect of dimming and smaller angular size caused by higher redshifts, in addition to the effect of the rest waveband shift, simple rescaling and rebinning of the real data will not work, because these manipulations will again produce the incorrect amount of noise.

To circumvent most of these challenging problems, Hashimoto et al. (2007) developed a very useful simulating technique employing a series of ‘adaptive scalings’ accompanied by a noise adding process applied to the real images. This technique, which can be used for all kind of imaging data, including optical, NIR, and X-ray images, allows us to simulated an image of desired exposure time and redshift with correct signal-to-noise ratio. Here we briefly describe the method, but please see Hashimoto et al. 2007 for further discussion and details.

To simulate data with integration time  $t_1$ , an original unsmoothed image (containing the background) taken with original integration time  $t_0$  was first rescaled by a factor  $R_0/(1-R_0)$ , instead of simple  $R_0$ , where  $R_0=t_1/t_0$ ,  $t_0>t_1$ . That is, an intermediate scaled image  $I_1$  was created from the original unsmoothed image  $I_0$  by:

$$I_1 = I_0 \frac{R_0}{(1-R_0)}. \tag{1}$$

Poisson noise was then added to this rescaled image by taking each pixel value as the mean for a Poisson distribution and then randomly selecting a new pixel value from that distribution. This image was then rescaled again by a factor  $(1-R_0)$  to produce an image whose *signal* is scaled by  $R_0$  relative to the original image, but its *noise* is approximately scaled by  $\sqrt{R_0}$ , assuming that the intrinsic noise initially present in the real data is Poissonian.

Similarly, to simulate the dimming effect by the redshift, an intermediate scaled image  $I_1$  is created from the background subtracted image  $I_0$  by a pixel-to-pixel manipulation:

$$I_1(x, y) = \frac{I_0(x, y)^2 R_1^2}{[I_0(x, y)R_1 + B - R_1^2(I_0(x, y) + B)]} \tag{2}$$

where

$$R_1 = [(1+z_0)/(1+z_1)]^4 \tag{3}$$

where  $z_0$  and  $z_1$  are the original redshift and the new redshift of the object, respectively, and  $B$  is the background.

Finally, to simulate the angular-size change due to the redshift difference between  $z_0$  and  $z_1$ , the original image will be rebinned by a factor  $R_2$ , [i.e.  $R_2=$  (angular-size at

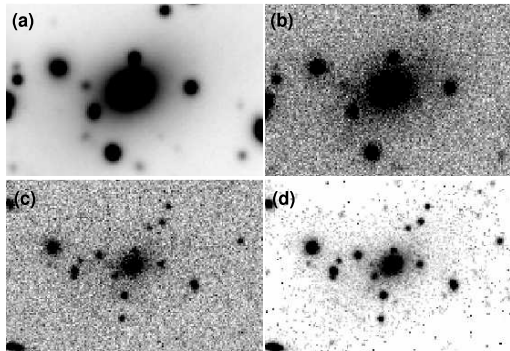


**Figure 1.** Simulating an image with desired exposure time and redshift using the real data: Even simulating an image with prolonged exposure time is possible with our adaptive scaling method. Here, optical R band images, taken with Subaru Suprime-Cam, around the center of an example cluster (Abell 2219) are shown. Images with original and modified exposure time and redshift are presented with north is up and east is left. (a) Original image: exptime( $t$ )=240s, and redshift( $z$ )=0.228, (b) Simulated shorter exposure image with  $t=10$ s (c) Simulated high- $z$  image with  $z=0.9$ ,  $t=240$ s (d) Simulated prolonged exposure at high- $z$  with  $t=1092$ s,  $z=0.9$

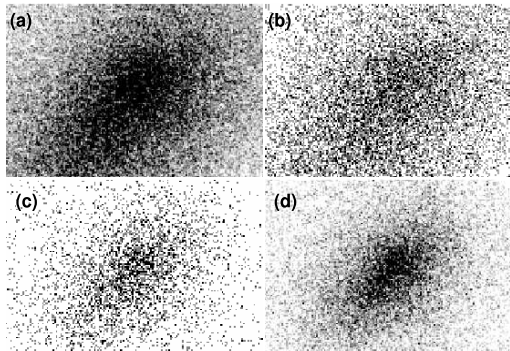


**Figure 2.** Similarly with Fig. 1, X-ray images from Chandra ACIS, of Abell 2219 are shown with original and modified exposure time and redshift. North is up and east is left. (a) Original:  $t=41$ ks,  $z=0.228$  (b) Simulated shorter exposure:  $t=10$ ks ( $z=0.228$ ) (c) Simulated high- $z$  image:  $z=0.9$  ( $t=41$ ks) (d) Prolonged exposure at high- $z$ :  $t=188$ ks,  $z=0.9$

$z_0)/(\text{angular-size at } z_1)]$ , then intermediate scaled image will be created by rescaling the rebinned image by a factor  $1/(R_2^2-1)$ , before the addition of the Poisson noise. For the simulation with ‘increased’ exposure time, this factor can be changed to  $R_3/(R_2^2-R_3)$  where  $R_3 = t_2/t_0$ ,  $t_2 > t_0$ , where  $t_2$  is the increased exposure time, and  $t_0$  is the original integration time, and  $(R_2^2 - R_3) > 0$ .

Although we suspected that our various measurements were quite robust, as a precaution we investigated the possible systematics on these measures introduced by various exposure times and redshifts, using our scaling technique described above.

In Fig. 1, we demonstrate our technique of simulating desired exposure time and redshift using the real optical image around the BCG at the cluster center taken with Subaru Suprime-Cam. Original and modified exposure time

and redshift of an example cluster (Abell 2219) are shown with north up and east left, where (a) original image: exptime( $t$ )=240s, and redshift( $z$ )=0.228 ( $\sim 20'' \times 35''$  area is displayed here), (b) simulated shorter exposure image with  $t=10$ s, (c) simulated high- $z$  image with  $z=0.9$ ,  $t=240$ s, and (d) simulated prolonged exposure at high- $z$  with  $t=1092$ s,  $z=0.9$ .

Similarly, in Fig. 2, we use the real X-ray images of Abell 2219 from Chandra ACIS, and simulated various exposures and redshifts, where (a) original image with  $t=41$ ks,  $z=0.228$  ( $\sim 100'' \times 175''$  area is displayed here), (b) simulated shorter exposure:  $t=10$ ks ( $z=0.228$ ), (c) simulated High- $z$  image:  $z=0.9$  ( $t=41$ ks), and (d) prolonged exposure at High- $z$ :  $t=188$ ks,  $z=0.9$ .

Using this technique, we simulated datasets with various exposure times and redshifts, and measured our cluster and galaxy parameters. We found that our X-ray and optical measures, at least of a single object, were quite robust against various exposure times and redshifts. For more detail, please see Hashimoto et al. (2007). For the influence from the neighboring objects and minimum number of pixel will be further discussed in the section 4.2.

## 4.2 Deblending and Minimum Number of Pixel

Our measures proved to be relatively independent of the direct influence from the variation of data quality. However, for measuring galaxy morphology, it can be easily speculated that a threshold related to minimum number of pixel of galaxy should be introduced. This threshold, however, actually consists of two types. The first type is the threshold to deal with the the direct effect from the small number of pixel (npix) of a single galaxy. The level of the threshold of this type is dependent on the particular morphological measure. We find that, in general, the measures such as concentration index require the largest threshold (npix  $\sim 100$ ). The second type of the threshold is to deal with the indirect influence related to the ‘deblending’ of multiple galaxies. This type of threshold is comparatively less recognized, therefore further explanation is necessary.

Suppose that we have an imaginary pair of galaxies in simulation whose intrinsic characteristics (such as physical size, absolute magnitude, or intrinsic colour) remain constant while we move the pair across a range of redshifts during the simulation. Apart from the effect of ‘ $k$  correction’, as the redshift of the pair changes, the apparent brightness (relative to the background noise) and the angular size of each individual galaxy also changes. In addition, the angular separation of the pair becomes smaller and this small angular separation (relative to the size of resolution elements or seeings) and small apparent size of each galaxy will ‘smooth’ the light distribution and it reduces the relative ‘contrast’ of two galaxies. Similarly, any type of variations in the data quality, such as lower spatial resolution or lower signal-to-noise, can cause similar changes in those four characteristics (i.e. the apparent brightness and angular size of each galaxy, and the angular separation and relative contrast of the pair).

Unfortunately, our ability to separate the pair galaxies from each other, i.e. ‘deblending ability’ in an image detection algorithm is predominantly dependent on these four characteristics. Therefore, variations in redshifts or data quality will cause the variations in the ‘deblending’ of galax-

ies, and thus may indirectly affect the morphological measures. For example, if you have two neighbouring ‘undistorted’ galaxies, and bring them to a high redshift or degrade the image quality, they start to resemble a single big morphologically ‘distorted’ galaxy, instead of two separate normal looking galaxies. This effect is unfortunately not unique to our morphological measures, but can occur at any qualitative or quantitative investigations of morphology.

One can improve the deblending performance by using data of better image quality (such as higher spatial resolution and/or deeper exposure). Similarly, one can improve the performance by changing the deblending parameters in the detection algorithm. However, this ‘improved’ deblending will again encounter the same deblending problem at more subtle deblending conditions (such as the smaller apparent separation of two galaxies). Furthermore, it is fundamentally not trivial, therefore somewhat arbitrary, to determine the optimal deblending performance. Namely, it is not trivial to determine if an object is really composed of two galaxies or a single morphologically disturbed galaxy with two cores.

Fortunately, we only have two deblending statuses, i.e. ‘deblended’ or ‘blended’, therefore the effect of ‘deblending capability’ should remain roughly constant down to a certain ‘deblending limit’, then it drops. (Therefore, even if we apply a significant deblending, it will not change our morphological measures much compared to the ‘optimal’ deblending, unless we do it to extremes, where the algorithm starts to deblend small intra-galactic structures.) Furthermore, this ‘deblending capability’ can be roughly characterized by the apparent size of object (e.g. number of pixel of a galaxy), because the average surface density (therefore, the average separation) of galaxies is related to apparent magnitude of galaxies, and this magnitude is approximately correlated to the number of pixel of galaxy.

When we plot the mean value of each measure versus the number of pixel of an object inside the entire image, one can find that the mean value is more or less flat down to a certain number of pixel, then object consists of smaller number of pixel starts to show much different (usually bigger) mean value of the morphological measure. The effect of the deblending on the minimum number of pixel can be best characterized by the ellipticity or PW2/PW0, and for the nominal setting for the deblending in your image extracting software, the threshold should be set around npix=50.

Now, this threshold related to the deblending is bigger than previously explained threshold related to the single object for the measure such as ellipticity and PW2, but we find that it is smaller than the single object threshold for measures such as the concentration and asymmetry. Note that the single object threshold is, as explained earlier in the section, variable among different measures. Instead of applying measure-by-measure threshold, we decided to apply one generic threshold (npix=100) for all measures, estimated according to the measure that requires the largest minimum number of pixel.

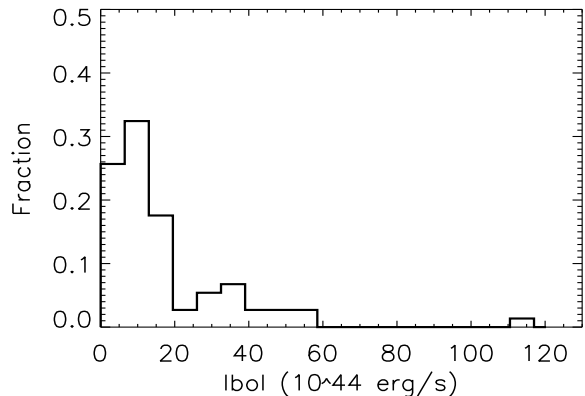


**Figure 3.** Distribution of the X-ray bolometric luminosity ( $L_{bol}$ ) for our cluster sample.

## 5 RESULTS

### 5.1 Distributions of X-ray Characteristics of Clusters

Figure 3 shows the distribution of X-ray bolometric luminosity of our cluster sample. The luminosity ranges between  $1.0 \times 10^{44} - 1.2 \times 10^{46} \text{ erg s}^{-1}$  (median  $8.56 \times 10^{44} \text{ erg s}^{-1}$ ), while Figure 4 and 5 show distributions of cluster X-ray morphology in the Cx (concentration) vs. Ax (asymmetry) plane, and Cx vs. Ex (ellipticity) plane, respectively. One sigma errors are approximately estimated from the Monte Carlo simulation. Note that entire X-ray sample of Hashimoto et al. (2007) is plotted here. In Fig. 4 and 5, we can see that clusters are scattered in the morphological planes, showing various morphological characteristics. However, there is a strong to weak correlation between Cx and Ax, and Cx and Ex with the value of Spearman  $\rho = -0.52$  and  $-0.36$  (significant at significance level =  $1.77 \times 10^{-9}$  and  $4.95 \times 10^{-5}$ ), respectively. These trends indicate that low concentration clusters generally show high degree of asymmetry, or ellipticity, illustrating the fact that there are not many highly-extended diffuse clusters with symmetric round profiles. Note that Fig. 5 shows a weak correlation between Ex-Cx. We suspect that this trend is due to the intrinsic nature of cluster morphology, and not due to the projection effect, because our concentration index is quite robust against the variation caused by the projection effect. We will further investigate this issue in detail in Sec. 5.3.

### 5.2 Distributions of Optical Characteristics of BCGs

Figure 6 shows the distributions of BCG morphology of our sample clusters in the  $A_g$  (asymmetry) -  $C_g$  (concentration) (top panel) plane, and  $E_g$  (ellipticity) -  $C_g$  (bottom panel) plane in the detection bands. In Figure 6, BCGs (marked by open circles) of our sample clusters are showing a wide variety of morphology in the  $A_g$ - $C_g$  and  $E_g$ - $C_g$  planes. One sigma errors are approximately estimated from Monte Carlo simulations. For comparison, the red sequence galaxies are also plotted (red dots) in Figure 6. For brevity, and so the number galaxies are comparable to BCGs, the red sequence

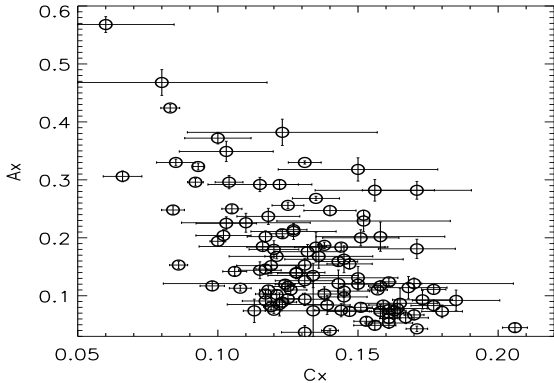


**Figure 4.** The distribution of Concentration and Asymmetry of cluster X-ray profile for our cluster sample.

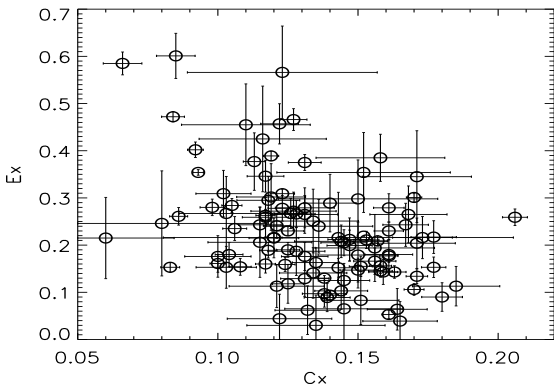


**Figure 5.** The distribution of Concentration and Ellipticity of cluster X-ray profile for our cluster sample.

galaxies are randomly selected from several randomly selected clusters. The red sequence galaxies are selected using the color magnitude diagram, as galaxies brighter than the BCG magnitude + 3 and  $\pm 0.1 \times (B-R)$  or  $(V-I+)$  at either side of the semi-manually fitted red sequence line. On contrary to the naive expectation that BCGs may resemble early type galaxies, BCGs seem to show a wider variety of morphology, particularly in  $C_g$  or  $A_g$  space. A K-S test shows that probability that distributions of BCGs and red sequence galaxies are drawn from the same parent distribution is  $4.14 \times 10^{-5}$  and  $7.59 \times 10^{-5}$ , for  $C_g$  and  $A_g$ , respectively.

In Figure 7, the morphological distributions of the second brightest galaxy (BCG2), and the third brightest galaxy (BCG3) inside the projected radius of 0.5 Mpc from the X-ray center are shown. BCG2 and BCG3 are then visually inspected and the assignments are adjusted, if needed, based on their colours and the distance to the X-ray center, as well as the redshifts if available in the literature. Similarly to Figure 6, the red sequence galaxies are also plotted for comparison. BCG2 galaxies seem to show a similar morphological distribution with BCGs, showing a wider morphological variation than the red sequence galaxies. A K-S test shows that probability that distributions of BCG02s and

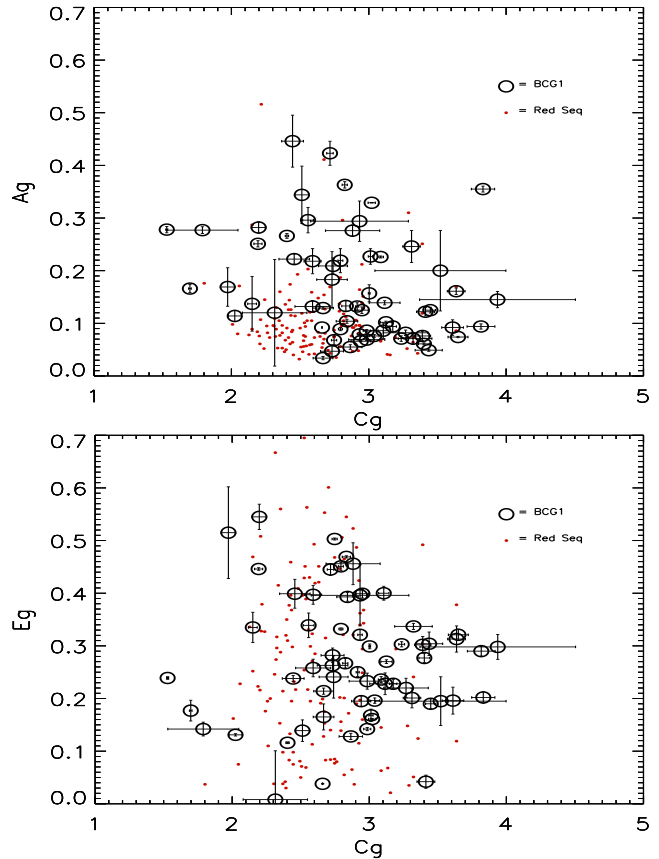


**Figure 6.** Distribution of BCG (marked by open circles) morphologies in the  $A_g$ - $C_g$  (top) and  $E_g$ - $C_g$  (bottom) planes. For comparison, the randomly selected red sequence galaxies are plotted (red dots).

red sequence galaxies are drawn from the same parent distribution is  $2.61 \times 10^{-6}$  and  $1.25 \times 10^{-5}$  for  $C_g$  and  $A_g$ , respectively. Meanwhile, BCG3 galaxies seem to show more or less similar morphology with BCG2, but show a hint of slightly less clear segregation in  $A_g$  from the red sequence galaxies. A K-S test shows that probability that distributions of BCG03s and red sequence galaxies are drawn from the same parent distribution is  $2.61 \times 10^{-6}$  for  $C_g$ , and  $4.48 \times 10^{-4}$  for  $A_g$ . The result seems to suggest that there is a continuous variation of morphology between BCG, BCG2, and BCG3, rather than a clear sharp separation of morphological characteristics between the BCG and the rest of the bright galaxies.

Meanwhile, in Figure 8, the distributions of other morphological measures of BCGs, Contrast vs. Ellipticity (top panel) and  $PW4/PW0$  vs.  $PW1/PW0$  (bottom panel) are plotted. Please note that dipole moment  $PW2$  and  $PW3$  are omitted, because they are very similar to ellipticity and asymmetry, respectively, by definition.

### 5.3 Brightest Cluster Galaxy and X-ray Characteristics of the Host Cluster

Figure 9 shows the distance of the BCG to the center of cluster, expressed in the unit of cluster major axis, plotted against the ellipticity of cluster X-ray profile. The cluster

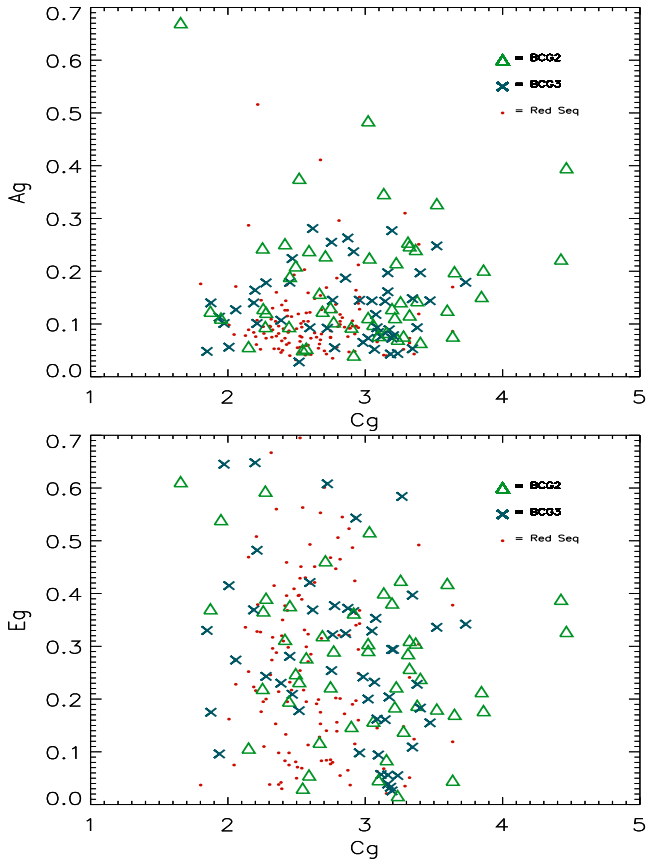


**Figure 7.** Distributions of morphologies of the second brightest galaxy (BCG2; triangle), and the third brightest galaxy (BCG3; x ) inside the projected radius of 0.5 Mpc from the X-ray center are shown. Similarly to Figure 6, the red sequence galaxies are also plotted for comparison.

major axis is measured from the X-ray emission, while the BCG position is determined in the optical detection band. The cluster center here is determined by the ‘4th order’ of the centroid of the X-ray emission, to minimize the influence from faint outer X-ray structure (c.f. Hashimoto et al. 2007). One sigma errors on BCG offset are estimated from Monte Carlo. It appears in Figure 9, that there is a weak trend in such way that clusters with high X-ray ellipticity show large BCG offsets (Spearman  $\rho = 0.41$ ; significance level =  $9.8 \times 10^{-4}$ ).

However, Figure 9 should be interpreted with caution, because both the ellipticity and BCG offset can be influenced by the cluster projection effect on the plane perpendicular to the line of sight. Fortunately, even from a simple geometrical argument, one can estimate that the probability of creating the clusters with apparent low projected ellipticity out of high intrinsic ellipticity is rather low, and therefore the bulk of the clusters maintains similar or only slightly lower ellipticity than the original ellipticity. Exactly the same geometrical argument is applicable to the offset of the BCGs.

To ensure that even this small probability will not create any artificial trend, we performed Monte Carlo simulation. Figure 10 shows the BCG distance to the cluster center for the simulated clusters versus projected cluster ellipticity. Here, cluster shape is assumed to be ellipsoidal

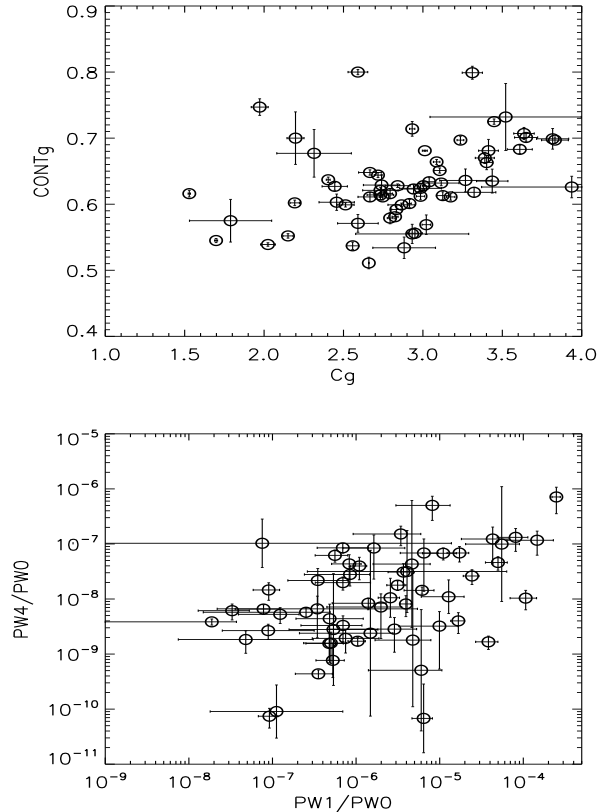


**Figure 8.** Distribution of BCGs in the planes of further morphological measures: Contrast vs. Ellipticity (top panel) and  $PW4/PW0$  vs  $PW1/PW0$  (bottom panel).

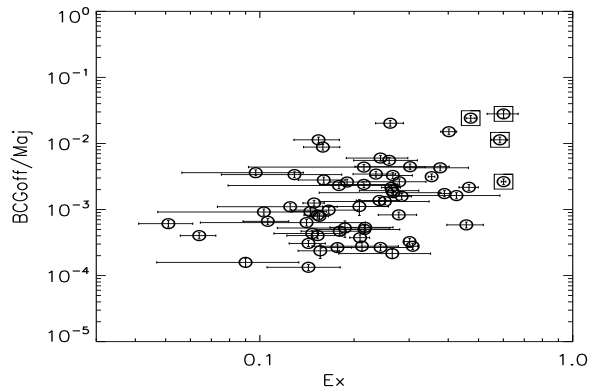


**Figure 9.** The BCG offset from the cluster center versus the ellipticity of cluster X-ray profile. The BCG offset is expressed in the unit of cluster major axis. The squares denote obvious double clusters.

with NFW (Navarro-Frenk-White; Navarro et al. 1996) profile with  $R_s=0.5$ . The original ellipticity of the cluster (i.e. the maximum projected ellipticity of the ellipsoid ) is chosen randomly between 0.05 and 7, then the ellipsoid is randomly oriented with respect to the line of sight. In the top panel, the initial position of BCG is randomly chosen inside the entire ellipsoid, while in the bottom panel, the position of

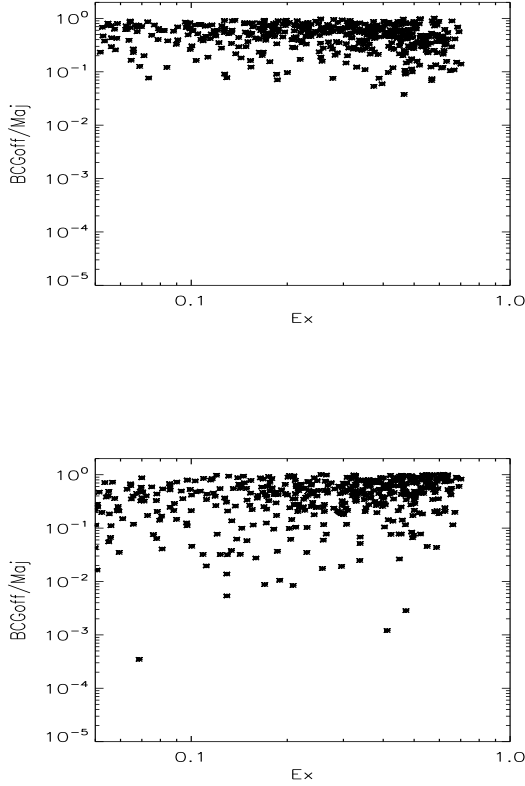


**Figure 10.** Simulated projection effect on the BCG offset vs X-ray ellipticity. Cluster shape is assumed to be ellipsoidal with NFW profile. The original ellipticity of the cluster (i.e. the maximum projected ellipticity of the ellipsoid) is chosen randomly between 0.05 and 0.7. In the top panel, the position of BCG is randomly chosen inside the ellipsoid, while in the bottom panel, the position of BCG is chosen randomly *only* along the major axis of the ellipsoid. No trend between BCG offset and the ellipticity the cluster morphologies can be generated from the random projection effect of clusters, even if we let the projection effects act on the ellipticity and BCG position in a correlated manner.

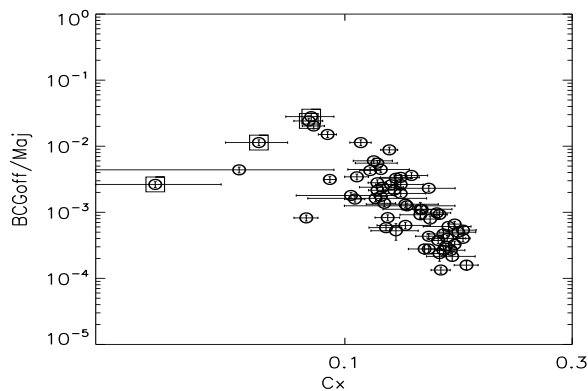


**Figure 11.** The BCG offset (in the unit of the cluster major axis) versus the concentration index of cluster X-ray profile.

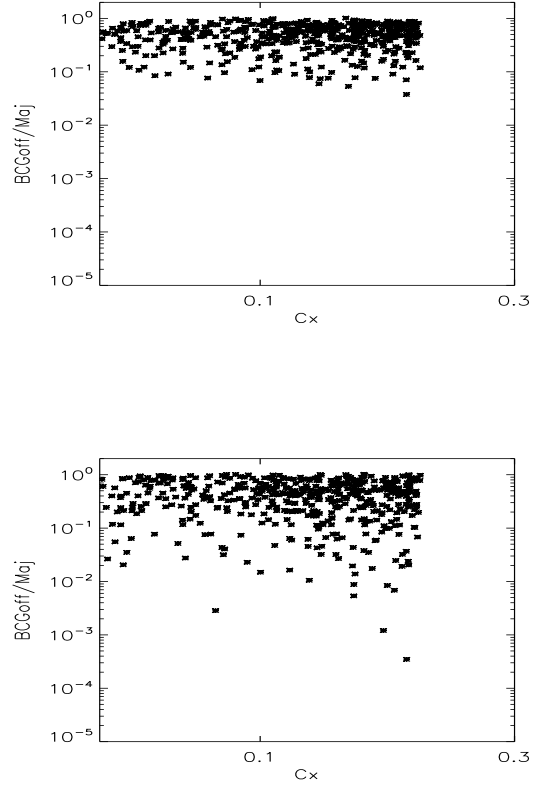


**Figure 12.** Simulated projection effect on the BCG offset vs X-ray concentration. Initial input concentration is chosen randomly between 0.05-0.2. The position of the BCG is chosen randomly inside the ellipsoidal cluster (top panel), and is chosen randomly *only* along the major axis of the ellipsoid (bottom panel). No trend between BCG offset and the concentration can be generated from the random projection effect of clusters,

BCG is allowed to vary randomly *only* along the major axis of the clusters. In total, 500 such random clusters are generated, for each panel. Figure 10 shows that, even if we let the projection effects act on the ellipticity and BCG position in a correlated manner, the projection effect alone cannot produce the trend between BCG offset and the ellipticity of the cluster X-ray morphologies.

In Figure 11, we plotted the BCG offset, again measured in a unit of the cluster semi-major axis, against the cluster X-ray concentration ( $C_x$ ) for our real sample. The concentration, just as the ellipticity, is expected to be sensitive to the cluster morphological distortion related to dynamical status of clusters, yet our concentration, unlike the ellipticity, is designed to be much more robust against projection effect, because we define the concentration independent of the shape of the ellipsoid. Figure 11 shows a clear trend between the BCG offset and  $C_x$  of cluster (Spearman  $\rho = -0.80$ ; significance level =  $3.25 \times 10^{-15}$ ) that is consistent with the scenario that the BCG position may be related the dynamical status of clusters (e.g. Ostriker & Tremaine 1975; Merritt 1985; Katayama et al. 2003).

In Figure 12, we further tested the projection effect on

the concentration. In Figure 12, original input concentration is chosen randomly between 0.05. and 0.2. Figure 12 shows that, as expected from the definition of the concentration, the concentration index hardly changes (except for induced small random scattering) by random orientation of the clusters, and we cannot generate any apparent correlation between BCG offset and the concentration by the projection effect alone, in the both cases of the random BCG position inside everywhere in the ellipsoid (top panel), and the random BCG position along the major axis of the ellipsoid (bottom panel).

Three clusters at the high end of cluster X-ray ellipticity ( $E_x$ ) in Fig. 9, and the low end of cluster X-ray concentration ( $C_x$ ) in Fig. 11, are “double” clusters that is two clusters that appear to merge into one cluster (marked by squares in both Fig. 9 and 11. In these double clusters, in extreme case, even if we have a BCG in each of two clusters and each BCG is nicely aligned to the center of each cluster, the cluster morphological measures and cluster center, based on the entire (double) cluster, (and choosing only one BCG per cluster), may not be able to differentiate this ‘each-lobe alignment’ from the whole cluster alignment. Note, however, that since there is no objectively clear ‘boundary’ between one semi-double lobe cluster and two colliding clusters, enforcing arbitrary separation of two types of clusters may artificially introduce some discontinuity in the analysis, and therefore in our understanding of the cluster morphology. Whether or not one should treat double clusters as one cluster or separating each lobe into two clusters is not at all a trivial problem.

One more caution should be exercised in interpreting Figure 9 and 11. There is some possibility that x and y axes in the figures are not completely independent. Namely, one can expect that, when cluster morphology gets highly distorted, it does not often maintain the simple distorted morphology, and that complex morphology may lead to a lack of obvious center. Even if our centering algorithm can still define the center well in unambiguous manner for these clusters with complex morphology, it may not be trivial to relate the measured center to a dynamically important center (e.g. center of gravity defined by dark matter, or center in the momentum space). This ‘uncertainty’ in determining the cluster center may indirectly affect the measurement of the BCG offset. Note that this effect on the measurement of the BCG offset, if any, is expected to mostly increase the scattering of the measured BCG offset, and not to shift the offset, directly. However, if the BCG offset is intrinsically very small compared to the size of the scatter, this scatter in the offset may shift the mean offset to slightly higher value, because we have no negative value for the offset (i.e. the scatter *into* the negative value is ‘folded’ to positive value). Now, this scatter can be larger for increasing cluster X-ray distortion, therefore if the underlying BCG offset is intrinsically small, the scattering effect on the offset may slightly enhance the X-ray morphology vs. BCG offset trend. However, in significant fraction of clusters, where one can define the cluster center unambiguously, even if the morphology is distorted (e.g. nice symmetrical ellipse), the BCGs still tend to be located at a large offset from the cluster center, and follows the overall trend in the offset related plots without any ‘discontinuity’ between these clusters and other more complex looking clusters. Finally, even if the small part of

the offset trend is indeed due to the ‘scattering effect’, the fact remains that both BCG offset and the cluster X-ray morphology are comparable measures in sense of characterizing possible dynamical status of clusters.

In Figure 13, we plot the optical luminosity of the BCGs (one from each cluster) versus X-ray bolometric luminosity ( $L_x$ ) of the host cluster (top panel), and versus X-ray temperature ( $T_x$ ) of the cluster (bottom panel). The BCG luminosity is calculated based on the k corrected R magnitude. Note that clusters without R band data are excluded in the figure, to reduce additional scatter associated with relative k correction error between different bands.  $L_x$  errors are assumed to be 10% error for clusters without estimated errors. Both panels, in particular the top panel, show that there is a weak trend that high  $L_x$  or  $T_x$  clusters harbour brighter BCGs, although the scatter is large (Spearman  $\rho$  is 0.43 and 0.18, significance level =  $6.2 \times 10^{-3}$  and  $2.7 \times 10^{-1}$  respectively for the top panel and the bottom panel). The result is in agreement with previous works reporting similar weak correlations between X-ray properties and optical BCG luminosity (e.g. Schombert 1987; Edge & Stewart 1991; Brough et al. 2002; Katayama et al. 2003).

To investigate the origin of the scattering in Figure 13, we show the subset of clusters according to their X-ray morphology in Figure 14, where the open squares represent clusters with highly distorted X-ray morphology ( $C_x < 0.11$  or  $A_x > 0.21$ ) and the solid circles represent clusters with very undisturbed X-ray morphology ( $C_x > 0.13$  and  $A_x < 0.13$ ). In Figure 14, it seems that clusters with very settled appearance tend to harbour the brighter BCGs compared to clusters very disturbed appearance. Namely, the BCG luminosity correlation with cluster luminosity or temperature seems to consists of two stronger parallel correlations for disturbed and undisturbed clusters. A K-S test along the BCG luminosity shows that the probability that the two distributions are drawn from the same parent distribution is  $1.14 \times 10^{-3}$ .

To further investigate this trend of dynamical influence in Figure 14, we plotted the luminosity of BCGs against the offset of the BCGs from the X-ray center in Figure 15. The figure shows that BCGs at a larger offset from the X-ray center exhibit a larger variation in their luminosity, and this variation seems to be always at ‘fainter’ side of the luminosity. That is to say that the figure shows a weak trend, with considerable scatter, that the BCGs at smaller offset from the X-ray center are brighter on the average (Spearman  $\rho$  is -0.38, significance level =  $1.4 \times 10^{-2}$ ). The trends in both Figure 14 and 15 may support the idea that the cluster-cluster merger may not be negligible compared to the scenario of the early collapse, as the mechanism of BCG formation, however, the more detailed discussion will be presented in Sec. 6.

## 6 SUMMARY AND DISCUSSION

We report an investigation of the relationship between the clusters of galaxies and BCGs, in particular, between the dynamical status of the clusters and the properties of BCGs.

We find that: 1) BCGs show a wide variety of morphology in all of our objectively determined morphological measures. The variety is comparable to that of the bright

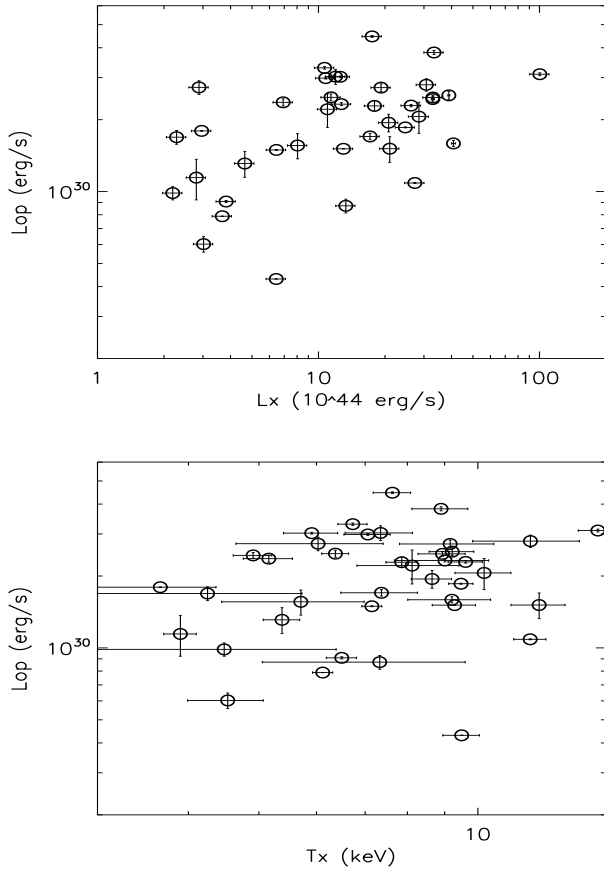


**Figure 13.** Luminosity of BCGs versus cluster X-ray bolometric luminosity (top), and versus X-ray temperature (bottom).

red sequence galaxies, except in the concentration versus asymmetry plane. The bright red sequence galaxies show a much more compact distribution of morphology in that plane. The second brightest, or the third brightest galaxies show a similar morphological variety compared to the bright red sequence galaxies in the concentration versus asymmetry plane, although the peak of distribution seems slightly off to the lower concentration values relative to that of the bright red sequence galaxies. The result seems to suggest that we have a continuous variation of morphology between BCG, BCG2, and BCG3, rather than a clear separation of morphological characteristics between the BCG and the rest of the bright galaxies. 2) The offset of the BCG position relative to the cluster center is correlated to the possible cluster dynamical status, defined by cluster X-ray properties, in such a way that, inside dynamically unsettled clusters, the BCGs tend to be more offset from the center of the global cluster potential well. 3) The luminosity of the BCGs are weakly correlated to the cluster X-ray luminosity or X-ray temperature, in a similar manner with cluster scaling relation, but with considerable scatter. The scatter seems to be much larger than the previously reported relationship between the BCG luminosity and X-ray luminosity or temperature, when the cluster sample extends beyond nearby X-ray bright clusters. 4) Effect of cluster dynamical status on the luminosity of the BCGs seems to be comparable to

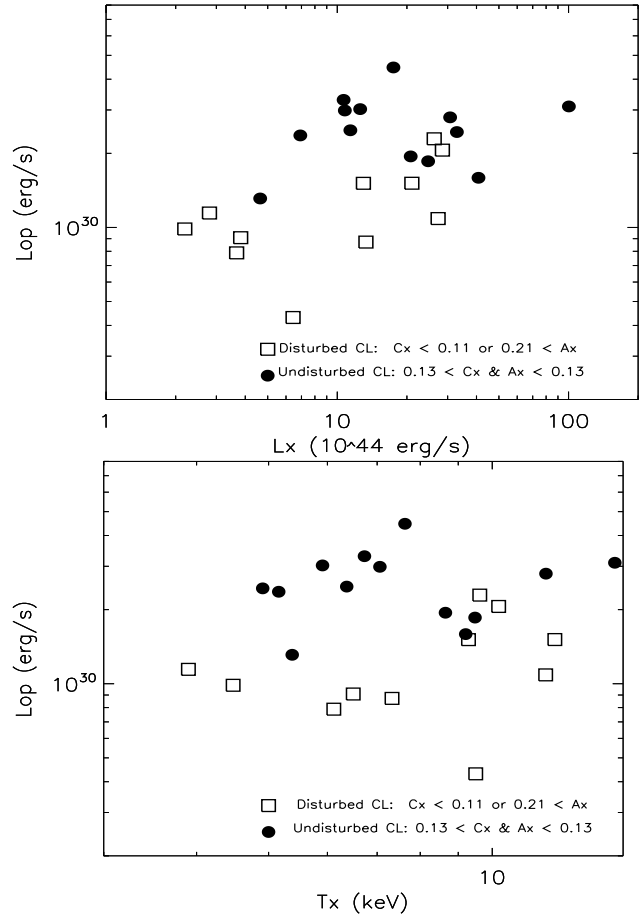


**Figure 14.** Luminosity of BCG versus cluster X-ray bolometric luminosity (top), and versus X-ray temperature (bottom) of subsets selected based on cluster dynamical status. Solid dots represent clusters with highly distorted X-ray morphology ( $C_x < 0.11$  or  $A_x > 0.21$ ) while open squares represent clusters with very undisturbed morphology ( $C_x > 0.13$  and  $A_x < 0.13$ ). The plots may imply that unsettled clusters may have fainter BCGs.

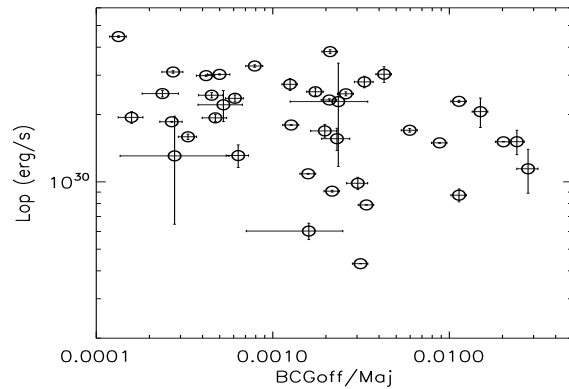


**Figure 15.** Luminosity of BCGs versus BCG offsets with respect to the cluster X-ray center.

the effect related to the cluster mass in such a way that the dynamically stable clusters tend to harbour brighter BCGs than those of unsettled clusters.

BCGs show morphology distinctively different from that of the bright red sequence galaxies in the Cg-Ag plane. The origin of this difference may be due to the fact that BCG galaxies tend to have many superposed small galaxies that BCGs are perhaps in the process of accreting, rather than the nature of BCGs themselves that may be altered by the influence of local environments on BCGs (e.g. Edwards & Patton 2012; Lidman et al. 2013; Burke & Collins 2013). Namely, if the differences we find about the BCGs are indeed due to the superposed small galaxies, then the difference between the BCGs and other bright galaxies can be attributed, if not all, to the ‘locational’ difference rather than the fundamental difference in the nature of the galaxies. That is to say, if we artificially superpose the image of, for example, the second or third brightest galaxies near the cluster center by bringing them from outskirts to the center, at least some, if not all, of the ‘BCG properties’ may be reproduced. This fact actually leads to a very fundamental problem that can apply to any study of very extended objects: there may be no fundamentally trivial way to decouple an object itself and its immediate surroundings, and perhaps it is necessary to understand them in one big picture of co-evolution of the object and the environments.

Our Figure 9 and 11 suggest that the BCG offset from the cluster center may be correlated to the cluster X-ray morphology. This result implies that the BCG offset from the cluster global potential well is sensitive to the cluster dynamical status, and that is consistent with previous studies investigating BCG offset from the optically determined cluster center among nearby clusters (e.g. Ostriker & Tremaine 1975; Merritt 1985; Katayama et al. 2003). However, just as other previous studies, the measurement of BCG offset may not be completely independent from the various measures characterizing the dynamical status of the clusters, i.e. two measurements are not completely orthogonal parameters, and therefore the physics behind the correlation between the BCG offset and the dynamical status of clusters should be interpreted with caution. Nevertheless, the fact remains that BCG offset can be a good measure to characterize the possible cluster dynamical status.

The fact that there is a weak correlation between the BCG luminosity and the X-ray luminosity or X-ray temperature of host cluster is consistent with previous studies reporting similar weak correlation between the X-ray cluster properties and BCG luminosity (e.g. Schombert 1987; Edge & Stewart 1991; Brough et al. 2002; Katayama et al. 2003; Stott et al. 2012). Our result is also in agreement with more traditional optical investigation where the BCG luminosity was compared to the optical properties of clusters (e.g. Oemler Jr 1976; Schombert 1987; Lin & Mohr 2004). The strengths of the correlations varied from one study to another, depending on the cluster measures and cluster samples of the study. Unfortunately, most of previous studies were predominantly using the low redshift bright cluster samples, that preferentially contained dynamically settled clusters. Therefore, the effect of cluster dynamical status on the luminosity (or other properties) of BCGs were hardly addressed.

Our Figure 14 shows that undisturbed looking clusters statistically harbour bright BCGs compared to those of disturbed clusters, implying that the effect of the dynamical status of clusters on the BCG luminosity may not be negligible. The result is qualitatively consistent with the previous studies revealing correlations between the ‘luminosity gap’ and cluster structure, where they reveal the trend that dynamically settled clusters tend to harbour dominant BCG (e.g. Smith et al. 2010; Chon et al. 2012).

Note that very high Cx clusters can contain ‘cool core’ clusters (e.g. Peterson & Fabian 2006). That is because of indirect selection effect that dynamically settled clusters tend to harbour the cool core, as well as the direct effect that Cx measure itself may be sensitive to the small scale X-ray profile associated with the cool core clusters near the center. This is the reason behind why the cluster morphology are characterized by both Cx and Ax in Figure 14 to minimize, at least, the direct influence from cool core using Cx alone.

Figure 15 is qualitatively consistent with Figure 14, in such a way that dynamically settled clusters tend to harbour brighter BCGs. Stott et al. (2012) reported a similar weak correlation between BCG optical luminosity and BCG offset, but with considerable scatter. This larger scatter is likely to be originated from the large uncertainty in determining their cluster centroids using shallow serendipitous observations with XMM-Newton.

What do these results in Figure 14 and 15 imply about the formation and evolution of BCGs? The popular scenarios of BCG formation and evolution are “galactic cannibalism” (e.g. Ostriker & Tremaine 1975; Malumuth & Richstone 1984), and “early collapse” (e.g. Merritt 1984). The fact that our BCG luminosity is correlated with cluster dynamical status may imply, at least, that the “early collapse” is not the only dominant mechanism to control the BCG formation and evolution.

However, it is pointed out that a simple galaxy-galaxy cannibalism scenario may require unusually short dynamical friction time scale to account for the observed large luminosity of BCGs (e.g. Merritt 1984). Indeed, Katayama et al. (2003) showed that, if their “virial density” could be interpreted as an age indicator of a cluster, BCG luminosity might not be correlated well to the age of the cluster, suggesting the possibility of being inconsistent with the simple galaxy-galaxy cannibalism scenario. Our dynamical indicators defined by X-ray morphology of clusters are expected to be more sensitive to a larger scale cannibalism, such as cluster-cluster merging, and may cover a longer evolutionary time scale than the “quiescent” age indicator, such as the virial density. We, therefore, suspect the fact that our BCG luminosity is correlated with our dynamical indicators does not support the simple galaxy-galaxy cannibalism model, but is more consistent with a larger/longer scale cannibalism as the mechanism of BCG formation and evolution, such as, cluster-cluster, or group-group merging, that can take place throughout the entire course of the cluster evolution even after the initial collapse (e.g. Lin & Mohr 2004).

Note however that, after the initial collapse of the BCGs, both cluster-cluster, and galaxy-galaxy cannibalisms can take place. To determine the relative importance of three different mechanisms: early collapse, galaxy-galaxy cannibalism, and cluster-cluster merger, the investigation of

the occurrence of distant “fossil groups” (e.g. Jones et al. 2003), or OLEG (X-ray overluminous elliptical galaxies) (Vikhlinin et al. 1999), as well as numerical simulation exploiting a wider parameter range of various merging scales, is much needed.

## ACKNOWLEDGMENTS

This work is based in part on data collected at Subaru Telescope and obtained from the SMOKA, which is operated by the Astronomy Data Center, National Astronomical Observatory of Japan. This research has made use of data obtained from the Chandra Data Archive, and software provided by the Chandra X-ray Center (CXC) in the application packages CIAO. We acknowledge the referee’s comments, which improved the manuscript. The work is partially supported by the National Science Council of Taiwan under the grant NSC 99-2112-M-003-001-MY2.

## REFERENCES

- Abraham R. G., Valdes F., Yee H. K. C., van den Bergh S., 1994, *ApJ*, 432, 75
- Bautz L., Morgan W., 1970, *ApJ*, 162, L149
- Beers T. C., Geller M. J., 1983, *ApJ*, 274, 491
- Bernardi M., Roche N., Shankar F., Sheth R., 2011, *MNRAS*, 412, L6
- Bertin E., Arnouts S., 1996, *A&AS*, 117, 393
- Bird C., 1994, *AJ*, 107, 1637
- Blanton M. R., Roweis S., 2007, *AJ*, 133, 734
- Böhringer H., Schuecker P., Guzzo L., Collins C. A., Voges W., Schindler S., Neumann D. M., Cruddace R. G., De Grandi S., Chincarini G., Edge A. C., MacGillivray H. T., Shaver P., 2001, *A&A*, 369, 826
- Brough S., Collins C., Burke D., Mann R., Lynam P., 2002, *MNRAS*, 329, 53
- Buote D., Tsai J., 1995, *ApJ*, 439, 29
- Buote D., Tsai J., 1996, *ApJ*, 458, 27
- Burke C., Collins C. A., 2013, *MNRAS*, 434, 2856
- Butcher H., Oemler A., 1978, *ApJ*, 226
- Butcher H., Oemler A., 1984, *ApJ*, 285
- Caldwell N., Rose J., Sharples R., Ellis R., Bower R., 1993, *AJ*, 106
- Carter D., Metcalfe N., 1980, *MNRAS*, 191, 325
- Chilingarian I., Melchior A., Zolotukhin I., 2010, *MNRAS*, 405, 1409
- Chon G., Böhringer H., Smith G. P., 2012, *A&A*, 548
- Conselice C. J., 2003, *ApJS*, 147, 1
- De Lucia G., Blaizot J., 2007, *MNRAS*, 375, 2
- Doi M., Fukugita M., Okamura S., 1993, *MNRAS*, 264, 832
- Dressler A., 1980, *ApJ*, 236, 351
- Dressler A., Shectman S., 1988, *AJ*, 95, 985
- Ebeling H., Edge A., Allen S., Crawford C., Fabian A., Huchra J., 2000, *MNRAS*, 318, 333
- Ebeling H., Edge A., Böhringer H., Allen S., Crawford C., Fabian A., Voges W., Huchra J., 1998, *MNRAS*, 301, 881
- Edge A., Stewart G., 1991, *MNRAS*, 252, 428
- Edwards L. O., Patton D. R., 2012, *MNRAS*, 425, 287
- Forman W., Jones C., 1982, *ARA&A*, 20, 547
- Geller M., Beers T., 1982, *PASP*, 94, 421
- Gerke B., Newman J., Faber S., Cooper M., Croton D., Davis M., Willmer C., Yan R., Coil A., Guhathakurta P., et al., 2007, *MNRAS*, 376, 1425
- Gioia I., Maccacaro T., Schild R., Wolter A., Stocke J., Morris S., Henry J., 1990, *ApJS*, 72, 567
- Gonzalez A. H., Zabludoff A. I., Zaritsky D., 2005, *ApJ*, 618, 195
- Goto T., Yamauchi C., Fujita Y., Okamura S., Sekiguchi M., Smail I., Bernardi M., Gomez P., 2003, *MNRAS*, 346, 601
- Hashimoto Y., Böhringer H., Henry J., Hasinger G., Szokoly G., 2007, *A&A*, 467, 485
- Hashimoto Y., Henry J., Böhringer H., 2008, *MNRAS*, 390, 1562
- Hashimoto Y., Oemler Jr A., 1999, *ApJ*, 510, 609
- Hashimoto Y., Oemler Jr A., Lin H., Tucker D., 1998, *ApJ*, 499, 589
- Henry J., Gioia I., Maccacaro T., Morris S., Stocke J., Wolter A., 1992, *ApJ*, 386, 408
- Jeltema T., Canizares C., Bautz M., Buote D., 2005, *ApJ*, 624, 606
- Jones C., Forman W., 1999, *ApJ*, 511, 65
- Jones L., Ponman T., Horton A., Babul A., Ebeling H., Burke D., 2003, *MNRAS*, 343, 627
- Jordi K., Ammon E., 2006, *A&A*, 460, 339
- Jorgensen I., Franx M., Kjaergaard P., 1992, *A&AS*, 95, 489
- Katayama H., Hayashida K., Takahara F., Fujita Y., 2003, *ApJ*, 585, 687
- Kolokotronis V., Basilakos S., Plionis M., Georgantopoulos I., 2001, *MNRAS*, 320, 49
- Kriessler J., Beers T., 1997, *AJ*, 113, 80
- Landolt A., 1992, *AJ*, 104, 340
- Lidman C., Iacobuta G., Bauer A., Barrientos L., Cerulo P., Couch W., Delaye L., Demarco R., Ellingson E., Faloon A., et al., 2013, *MNRAS*, 433, 825
- Lin Y., Mohr J., 2004, *ApJ*, 617, 879
- Malumuth E., Kriss G., Dixon W., Ferguson H., Ritchie C., 1992, *AJ*, 104, 495
- Malumuth E., Richstone D., 1984, *ApJ*, 276, 413
- Melott A., Chambers S., Miller C., 2001, *ApJ*, 559, L75
- Merritt D., 1984, *ApJ*, 276, 26
- Merritt D., 1985, *MNRAS*, 214, 25P
- Metevier A., Romer A., Ulmer M., 2000, *AJ*, 119, 1090
- Miyazaki S., Sekiguchi M., Imi K., Okada N., Nakata F., Komiyama Y., 1998, *Proc. SPIE*, 3355, 363
- Mohr J., Evrard A., Fabricant D., Geller M., 1995, *ApJ*, 447, 8
- Navarro J. F., Frenk C. S., White S. D. M., 1996, *ApJ*, 462, 563
- Oegerle W., Hill J., 2001, *AJ*, 122, 2858
- Oemler Jr A., 1976, *ApJ*, 209, 693
- Okamura S., Kodaira K., Watanabe M., 1984, *ApJ*, 280, 7
- Ostriker J., Tremaine S., 1975, *ApJ*, 202, L113
- Peterson J. R., Fabian A. C., 2006, *Phys.Rep.*, 427, 1
- Plionis M., 2002, *ApJ*, 572, L67
- Plionis M., Benoist C., Maurogordato S., Ferrari C., Basilakos S., 2003, *ApJ*, 594, 144
- Quintana H., Lawrie D., 1982, *AJ*, 87, 1
- Rhee G., van Haarlem M., Katgert P., 1992, *AJ*, 103, 1721
- Roche N., Bernardi M., Hyde J., 2009, *MNRAS*, 398, 1549
- Rood H., Sastry G., 1971, *PASP*, 83, 313

- Rosati P., Della Ceca R., Norman C., Giacconi R., 1998, ApJ, 492, L21
- Sanderson A., Edge A., Smith G., 2009, MNRAS, 398, 1698
- Schlegel D., Finkbeiner D., Davis M., 1998, ApJ, 500, 525
- Schneider D. P., Gunn J. E., Hoessel J. G., 1983, ApJ, 264, 337
- Schombert J., 1987, ApJS, 64, 643
- Schombert J. M., 1986, ApJS, 60, 603
- Schuecker P., Böhringer H., Reiprich T. H., Feretti L., 2001, A&A, 378, 408
- Smith G. P., Khosroshahi H. G., Dariush A., Sanderson A., Ponman T., Stott J., Haines C., Egami E., Stark D., 2010, MNRAS, 409, 169
- Stott J. P., Hickox R. C., Edge A. C., Collins C. A., Hilton M., Harrison C. D., Romer A. K., Rooney P. J., Kay S. T., Miller C. J., et al., 2012, MNRAS, 422, 2213
- Struble M., 1990, AJ, 99, 743
- Struble M., Rood H., 1984, AJ, 89, 1487
- Struble M., Rood H., 1987, ApJS, 63, 543
- Vikhlinin A., McNamara B., Forman W., Jones C., Quintana H., Hornstrup A., 1998, ApJ, 502, 558
- Vikhlinin A., McNamara B., Hornstrup A., Quintana H., Forman W., Jones C., Way M., 1999, ApJL, 520, L1
- von der Linden A., Best P. N., Kauffmann G., White S. D. M., 2007, MNRAS, 379, 867
- Yagi M., Kashikawa N., Sekiguchi M., Doi M., Yasuda N., Shimasaku K., Okamura S., 2002, AJ, 123, 66
- Yasuda N., Fukugita M., Narayanan V. K., Lupton R. H., Strateva I., Strauss M. A., Ivezić Ž., Kim R. S., Hogg D. W., Weinberg D. H., et al., 2001, AJ, 122, 1104
- Zabludoff A., Geller M., Huchra J., Vogeley M., 1993, AJ, 106, 1273